Numerical Simulation of Turbulent Flows in Complex Geometries Using the Coherent Vortex Simulation Approach Based on Orthonormal Wavelet Decomposition

Henning Bockhorn, Jordan A. Denev, Margarete Domingues, Carlos Falconi, Marie Farge, Jochen Fröhlich, Sônia Gomes, Benjamin Kadoch, Igor Molina, Olivier Roussel, and Kai Schneider

Abstract. Applications of the wavelet based coherent vortex extraction method are presented for homogeneous isotropic turbulence for different Reynolds numbers. We also summarize the developed adaptive multiresolution method for evolutionary PDEs. Then we show first fully adaptive computations of 3d mixing layers using Coherent Vortex Simulation. Features like local scale dependent time stepping are also illustrated and examples for one dimensional problems are given. Test cases on complex geometries like the periodic hill flow (with Reynolds numbers up to 37000) and an annular burner with a swirl number of $S = 0.6$ have been calculated based on the developed wavelet decomposition models. The extensive results presented show the robustness and good accuracy of the adopted wavelet approach for the various flows simulated.

1 Introduction

The present paper deals with analysis and simulation of complex turbulent flows and the utilization of the orthonormal wavelet decomposition for their study and computation. The first section presents an example of Coherent Vortex Extraction of three-dimensional isotropic turbulence from a Direct Numerical Simulation.

Even more than in the incompressible regime, the numerical simulation of fully–developed turbulent flows in the compressible regime is one of the challenges for

Henning Bockhorn
Institute for Technical Chemistry and Polymer Chemistry, University of Karlsruhe (TH), Kaiserstr. 12, 76128 Karlsruhe, Germany
`bockhorn@ict.uni-karlsruhe.de`

Kai Schneider
M2P2-CNRS & Centre de Mathématiques et d'Informatique, Université de Provence, 39 rue F. Joliot-Curie, 13453 Marseille cedex 13, France
`kschneid@cmi.univ-mrs.fr`

Marie Farge
LMD-IPSL-CNRS, Ecole Normale Superieure, 24, rue Lhomond, 75231 Paris Cedex 5, France
`farge@lmd.ens.fr`

scientific computing. The difficulty comes from the nonlinear dynamics of the Navier-Stokes equations, which excite a very large range of temporal and spatial scales. To perform computations in industrial configurations, turbulence models are necessary because Direct Numerical Simulation (DNS) of fully–developed turbulent flows is up to now limited to low Reynolds numbers. However, most turbulence models used in industrial codes are based on phenomenology, and thus require tuning of their parameters for each flow configuration. Coheren Vortex Simulation is a powerfull method which overcomes this principal difficulty of classical models and is demonstrated for the turbulent mixing layer in section 3.

Systems of nonlinear partial differential equations (PDEs) naturally arise from mathematical modelling of chemical-physical problems encountered in many applications, for instance in chemical industry. In turbulent reactive or non-reactive flow, for example, these PDE solutions usually exhibit a multitude of active spatial and temporal scales. However, as typically these scales are not uniformly distributed in the space–time domain, efficient numerical discretizations could take advantage of this property. Introducing some kind of adaptivity in space-time allows to reduce the computational complexity with respect to uniform discretizations, while controlling the accuracy of the adaptive discretization. The development and application of such an adaptive multiresolution method is shown in section 4.

An important step for the development of each numerical technology is the application toward real-life engineering applications. This presumes that the algorithm can easily be incorporated in existing codes for numerical simulations of flows with complex geometry. This step has been undertaken for the parallelized finite-volume code LESOCC2 developed for Large Eddy Simulations on curvilinear grids. The wavelet decomposition, implemented in this code has been tested extensively against other classical numerical models and experimental data. For this purpose test cases with high Reynolds numbers and complex geometry, developed within the present DFG-CNRS cooperation has been utilized. Results, showing the robustness and effectiveness of the wavelet algorithm as well as its good accuracy are presented in the last part of this work.

2 Coherent Vortex Extraction Using Wavelets

2.1 Principle

In the fully-developed turbulent regime one observes the emergence of coherent structures out of turbulent fluctuations. Typically, these structures are well localized and excited on a wide range of scales. Ten years ago Marie Farge and Kai Schneider have proposed a method, called Coherent Vortex Extraction (CVE), to extract them [11–13, 15, 32]. It decomposes turbulent fluctuations into two classes: coherent fluctuations, responsible of convective transport and incoherent fluctuations, responsible of diffusive transport. For this, they used the wavelet representation which presents the advantage, compared to the classical Fourier representation, to preserve both spectral and spatial structures. Their method relies on two original choices. The first one consists to represent turbulent fields using wavelets rather

than grid points (physical space representation) or Fourier modes (spectral space representation) as it is classically done. The second choice corresponds to a change of viewpoint. Since scientists working in turbulence have not yet agreed on a precise and operational definition of coherent structures, they have proposed the following minimalist definition : coherent structures are not noise. If one agrees on this hypothesis, the problem of extracting coherent structures becomes equivalent to denoising. Indeed, one no more needs hypothesis on structures themselves, but only on the noise to eliminate. To get started, they have proposed the simplest hypothesis about the noise, namely they have supposed the noise to be additive, white and Gaussian. This method is based on a wavelet decomposition of the vorticity field, a subsequent thresholding of the wavelet coefficients and a reconstruction from those coefficients whose modulus is above a given threshold. Wavelet bases are well suited for this task, because they are made of self-similar functions well localized in both physical and spectral spaces leading to an efficient hierarchical representation of intermittent data, as encounted in turbulent flows [11]. The value of the threshold is based on mathematical theorems yielding an optimal min-max estimator for the denoising of intermittent data [9, 10]. In this section we use the coherent vortex extraction (CVE) method and apply it to different realizations of homogeneous isotropic turbulent flows. They have been computed by direct numerical simulation (DNS), with a stochastic forcing at large scales, for a range of Reynolds number from $R_e = 20000$ to 400000 by P.K. Yeung and his group, from Georgia Tech (USA), who have kindly provided their data.

2.2 Coherent Vortex Extraction (CVE)

The CVE decomposition use an orthogonal three-dimensional multiresolution analysis (MRA) of $L^2(R^3)$ obtained through the tensor product of three one-dimensional MRA's of $L^2(R)$. In this context a function $f \in L^2(R^3)$ can be developed into a three-dimensional wavelet basis

$$f(\mathbf{x}) = \sum_{\gamma \in \Gamma} \widetilde{f}_\gamma \, \psi_\gamma(\mathbf{x}), \qquad \gamma = (j, i_x, i_y, i_z, \mu) \tag{1}$$

where j denotes the scale, $\mathbf{i} = (i_x, i_y, i_z)$ denotes the positions, $\mu = 1, ..., 7$ indicates the 7 wavelets and the index set $\Gamma = \{\gamma = (j, i_x, i_y, i_z, \mu) \quad j = 0, ..., J-1 \quad i_x, i_y, i_z = 0, ..., 2^j - 1 \quad \mu = 1, ..., 7\}$. Due to orthogonality the wavelet coefficients are given by $\widetilde{f}_\gamma = \langle f, \psi_\gamma \rangle$ where $\langle \cdot, \cdot \rangle$ denotes the L^2 inner product. For more details on this construction and in wavelets we refer the reader to the standard textbook [2] and also to the article [11] for the 3D case. Here the Coifman 12 mother-wavelet is chosen on the MRA. The reasons for this choise is that it is almost symmetric, it have compact support and there is a fast wavelet transform, $i.e.$, the total number of operations is $\mathcal{O}(N)$, where N is the resolution. Another important point is that this wavelet has $M = 4$ vanishing moments, and therefore the corresponding quadratic mirror filter has a length of $3M = 12$ [2]. The computational cost of the fast wavelet transform is of order CN, where N is the resolution, and C is proportional to the

filter length. Therefore the total number of operations is $O(N)$, while it is $O(N\log_2 N)$ for the Fast Fourier Transform (FFT) [14]. Therefore the total number of operations is $O(N)$, and is smaller than $O(N\log_2 N)$, the operation count for the fast Fourier transform, for $N > 2^{12} = 4096$.

We consider in the extraction algorithm a 3D vorticity $\omega = \omega(x,y,z)$ field $\omega = \nabla \times \mathbf{v}$, where $\mathbf{v} = \mathbf{v}(x,y,z)$ is the velocity field. The three components of ω are developed into an orthonormal wavelet series, from the largest scale $l_{max} = 2^0$ to the smallest scale $l_{min} = 2^{-J+1}$. The vorticity field is decomposed into coherent vorticity $\omega_c = \omega_c(x,y,z)$ and incoherent vorticity $\omega_i = \omega_i(x,y,z)$ by projecting its three components onto an orthonormal wavelet basis and applying nonlinear thresholding to the wavelet coefficients. The choice of the threshold is based on theorems [9, 10] proving optimality of the wavelet representation for denoising signals – optimality in the sense that wavelet-based estimators minimize the maximum L^2-error for functions with inhomogeneous regularity in the presence of Gaussian white noise. We have chosen the variance of the total vorticity (*i.e.*, twice the enstrophy Z) since we do not know *a priori* the variance of the noise. The threshold is then $T = (\frac{4}{3}Z\log N)^{\frac{1}{2}}$, where $Z = \frac{1}{2}\langle \omega, \omega \rangle$ is the total enstrophy and N^3 is the resolution. Notice that this threshold does not require any adjustable parameters.

In summary, we compute the modulus of the wavelet coefficients:

$$|\tilde{\omega}| = |\tilde{\omega}_\gamma| = \left(\sum_{n=1}^{3} \left[\tilde{\omega}_\gamma \right]_n^2 \right)^{\frac{1}{2}}. \tag{2}$$

Then, the coherent vorticity is reconstructed from the wavelet coefficients whose modulus is larger than the threshold T, while the incoherent vorticity is computed by the difference with the total field. The two fields thus obtained, ω_c and ω_i, are orthogonal, which ensures the decomposition of the total enstrophy into $Z = Z_c + Z_i$.

The CVE decomposition algorithm consists of three fast wavelet transforms (WT) for each vorticity component, a thresholding of the wavelet coefficients and three inverse fast wavelet transforms (IWT), one for each component of the $\tilde{\omega}_c$, *i.e.*, all coefficient with $|\tilde{\omega}|$ greater than the threshold, form the coherent vorticity (ω_c). The incoherent vorticity ω_i components are in principle computed using the inverse wavelet transform from the weak coefficients. In order to simplify computations we performed the difference between total and coherent vorticity
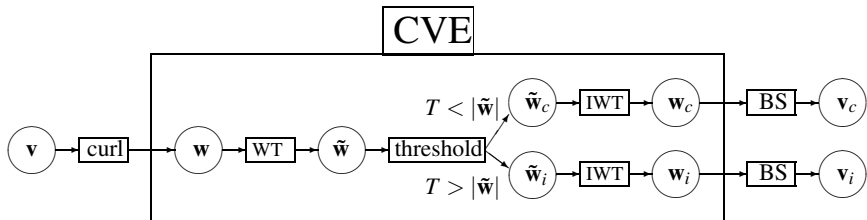

Fig. 1 Flowchart of CVE decomposition

which yields the same result. A flowchart of the CVE algorithm is depicted in Fig. 1. The induced coherent and incoherent velocity fields are computed using Biot–Savat's kernel (BS), $\mathbf{v} = \nabla \times (\nabla^{-2}\omega)$, from the coherent and incoherent vorticity fields, respectively.

2.3 CVE of Turbulent Flows at Different Reynolds Numbers

In the case of $N = 256^3$ we study the vorticity field, for the $N = 512^3$ and 2048^3 dataset, as they are are too large, we will only consider subcubes of 256^3.

Table 1 shows the statistical analysis comparing the total, coherent and incoherent flows for Reynolds number $R_e = 20000$ and Table 2 shows the same for 4 different 256^3 subcubes extracted from the $N = 512^3$ cube data set which correspond to a flow with Reynolds number $R_e = 60000$, and for 4 other different 256^3 subcubes of the $N = 2048^3$ cube which correspond to a flow with Reynolds number $R_e = 400000$. We found that the coherent flow corresponds to 3.6% of the wavelet coefficients and retains from 92.5% to 90.7% of the total enstrophy and more than 99% of the total energy. The remaining incoherent flow represents about 95% of the wavelet coefficients but retains from 7.5% to 9.2% of the enstrophy and less than 1% of the energy. A visualization of the modulus of vorticity and their coherent and incoherent contributions are shown in Figure 2. We observe that almost all

Table 1 CVE decomposition of a flow field computed at resolution $N = 256^3$ for Reynolds number $R_e = 20000$

	R_e=20000		
	total	coherent	incoherent
% of coefficients	100	3.59	96.41
Energy	2.955	2.946	0.004
% of Energy	100	99.7	0.14
min value	-5.92	-5.93	-0.31
max value	6.16	6.17	0.33
velocity skewness	0.1432	0.1439	0.0016
skewness	0.14317	0.14385	0.15956
velocity flatness	2.7818	2.7802	3.48
flatness	2.7818	2.7802	3.4816
Enstrophy	212.80	196.93	15.87
% of enstrophy	100	92.54	7.46
min value	-230.26	-243.29	-34.18
max value	245.86	259.24	38.19
vorticity skewness	-0.013	-0.016	$0.68 \cdot 10^{-3}$
vorticity flatness	8.08	8.31	4.92

Table 2 Statistical analysis of the CVE filtering of several vorticity fields computed at resolution $N = 256^3, 512^3, 2048^3$, which correspond to Reynolds number $R_e = 20000, 60000, 400000$ respectively

	R_e=60000			R_e=400000		
	total	coherent	incoherent	total	coherent	incoherent
subcube 1						
% of coeff.	100	3.64	96.36	100	3.69	96.31
Vorticity						
Enstrophy	598.51	550.76	47.75	4669.09	4418.81	450.27
% Enstrophy	100	92.2	7.98	100	90.75	9.25
Skewness	-0.046	-0.047	-0.001	0.067	0.076	-0.903
Flatness	10.42	10.88	5.32	13.23	14.17	5.72
subcube 2						
% of coeff.	100	3.66	96.34	100	6.62	93.38
Vorticity						
Enstrophy	685.12	624.41	60.7	5336.16	4856.18	479.98
% Enstrophy	100	91.14	8.86	100	91.01	8.99
Skewness	0.029	0.027	0.001	-0.483	-0.527	$-6.33\,10^{-06}$
Flatness	10.305	10.09	5.17	15.77	17.14	5.55
subcube 3						
% of coeff.	100	3.69	96.31	100	3.70	96.3
Vorticity						
Enstrophy	782.48	707.92	74.56	6975.17	6197.89	777.27
% Enstrophy	100	90.47	9.53	100	88.86	11.14
Skewness	0.157	0.164	0.001	0.05	0.544	$-3.50\,10^{-05}$
Flatness	10.77	11.41	5.25	14.08	15.39	5.88
subcube 4						
% of coeff.	100	3.66	96.34	100	3.69	96.31
Vorticity						
Enstrophy	738.75	673.21	65.54	6043.08	5426.71	616.37
% Enstrophy	100	91.13	8.87	100	89.8	10.2
Skewness	-0.14	-0.15	$-3.00\,10^{-04}$	-0.084	-0.0093	0.00002
Flatness	11.142	11.75	5.41	14.69	16.01	5.64
standard deviation						
% of coeff.	100	0.02061	0.02061	0	1.46334	1.46334
Vorticity						
Enstrophy	79.2048	68.1165	11.1797	987.662	768.802	149.519
% Enstrophy	0	0.71565	0.63597	0	0.97947	0.97947
Skewness	0.12544	0.13206	0.00099	0.25606	0.43885	0.45149
Flatness	0.37773	0.72315	0.10210	1.06849	1.2389	0.14008
mean						
% of coeff.	100	3.6625	96.3375	100	4.425	95.575
Vorticity						
Enstrophy	701.215	639.075	62.1375	5755.875	5224.8975	580.9725
% Enstrophy	100	91.235	8.81	100	90.105	9.895
Skewness	0	-0.0015	0.000175	-0.1125	0.020925	-0.225755333
Flatness	10.65925	11.0325	5.2875	14.4425	15.6775	5.6975

(a) $|\omega|$ (b) $|\omega_c|$ (c) $|\omega_i|$

$R_e = 20000$
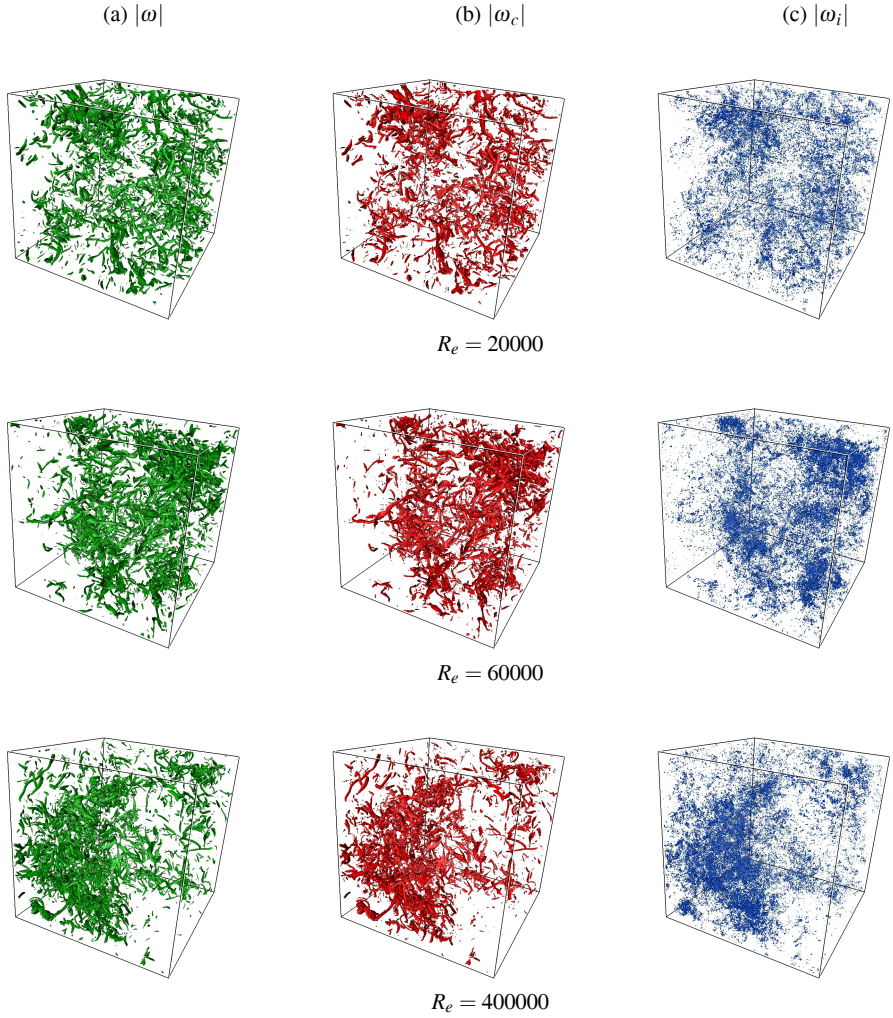

$R_e = 60000$

$R_e = 400000$

Fig. 2 Modulus of vorticity for (a), coherent part for (b), and incoherent part for (c).Note that for $R_e = 60000 and 400000$ subcubes 256^3 data set are visualized to zoom on the structures. The isosurface are $\sigma = 56, 96, 290$ for total and coherent parts and $\sigma = 14, 24, 75.2$ for the incoherent part, for $R_e = 20000, 60000, 400000$ respectively

structures are preserved in the coherent vorticity while they are no organized structures left in the incoherent vorticity. Indeed, the total and coherent vorticity fields present vortex tubes, while the incoherent vorticity looks structureless and noise-like. The vorticity PDFs and spectra for the total flow and for the coherent flow are similar, *i.e.*, non-Gaussian and long-range correlated, while the incoherent flow is decorrelated and has a much reduced variance (Fig. 3). We observe that all along the inertial range the coherent flow presents a similar energy and enstrophy spectra

$R_e = 20000$

$R_e = 60000$

$R_e = 400000$

(a) PDF of ω

(first 256^3 subcube)

(first 256^3 subcube)

(b) Enstrophy spectrum
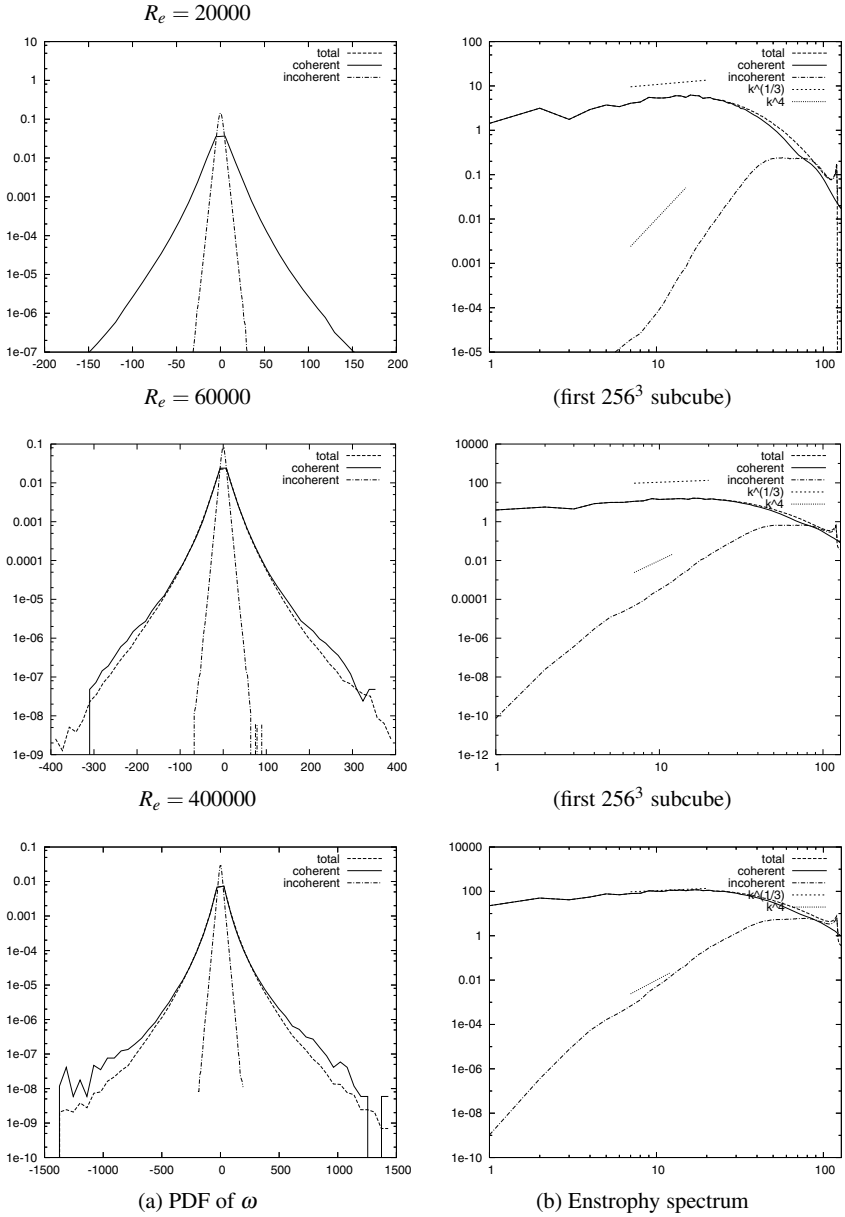
Fig. 3 PDF (left) of vorticity and entrophy spectrum (right) for the total field, coherent and incoherent parts for $R_e = 20000, 60000, 400000$

compared to the spectra of the total flow, whereas they differ only in the dissipative range for $k \geq 30$. The reconstruction of the coherent part of these fields requires only, for $R_e = 60000$, 3.6% of the wavelet coefficients and retains $\approx 92\%$ of the

enstrophy , and only $\approx 3.7\%$ of the wavelet coefficients maintains about 91% of the enstrophy for $R_e = 40000$. Additionally, there are nonsignificant changes in the skewness and flatness between the total field and the coherent field for the different R_e. Moreover we do not observe significant variations between the statistical properties of the four different subcubes for each for R_e.

The total, coherent and incoherent vorticity fields of the vorticity field is visualized in Figure 2 for $R_e = 20000, 60000, 400000$. As observed in the $R_e = 20000$, almost all structures are preserved in the coherent contribution and none remain in the incoherent contribution. However with the increase of R_e, we observe the presence of more structures in the analyzed subcubes.

In [26] the extraction of coherent structures is done for homogenous isotropic turbulent flows. A similar CVE is used for different resolutions $256^3, 512^3, 1024^3, 2048^3$ which correspond to $R_e = 30000, 70000, 200000, 600000$ respectively. The main difference is that the CVE is applied on all the fields and not on subcubes as we do here. The authors find that the compression rate increases with R_e. In our analysis on the subcubes, the compression rates are nearly constant $\sim 3.6\%$ for the different R_e $(20000, 60000, 400000)$, so that, the Donoho threshold increases with R_e. This could suggest that the compression rate is limited by the resolution, *i.e.*, the number of octaves available. Indeed the resolution of all cubes we analysed is constant at $N = 256^3$. Moreover the decay of wavelet coefficients is smaller for the subcubes, but the PDFs and spectra are very similar to the ones obtained in our study.

From the present results we conjecture that modelling the effect of the discarded modes on the resolved modes is easier to perform using the Coherent Vortex Simulation (CVS) approach introduced in [14]. CVS computes all degrees of freedom which contribute to the flow nonlinearity, *i.e.*, the coherent modes, whatever their scale, while the remaining degrees of freedom, *i.e.*, the incoherent modes, are discarded to model turbulent dissipation. The method actually combines an Eulerian projection of the solution with a Lagrangian procedure for the adaption of the computational basis: for more details we refer the reader to [14]. The next step to demonstrate the potential of CVS is to develop an adaptive wavelet solver for the 3D Navier–Stokes equations.

3 Coherent Vortex Simulation of Turbulent Mixing Layers

In this section, we present an extension of the Coherent Vortex Simulation (CVS) [14] method to compressible flows. The CVS method is based on the observation that turbulent flows contain both an organized part, the coherent vortices, and a random part, the incoherent background flow. The separation into coherent and incoherent contributions is done using a non-linear wavelet filtering. The evolution of the coherent part is computed in physical space using a finite volume scheme on a locally refined grid, while the incoherent part is discarded during the flow evolution, which models turbulent dissipation. To discretize the convective terms, we use a 2–4 McCormack scheme [17], while the diffusive terms are discretized using a second–order centered scheme in space. The time integration is done by an

Table 3 Comparison between DNS and CVS of a 3D compressible mixing layer, $Ma = 0.3$, $Re = 200$. CPU time required on a Pentium IV 2.5 GHz, percentages of CPU time, required memory, total energy E and total enstrophy Z in comparison with the DNS computation

Method	CPU time	% CPU	% Mem	% E	% Z
DNS	7 day 09 h 40 min 08 s	100.0 %	100.0 %	100.0 %	100.0 %
CVS	2 day 07 h 00 min 03 s	29.0 %	30.2 %	98.3 %	93.4 %
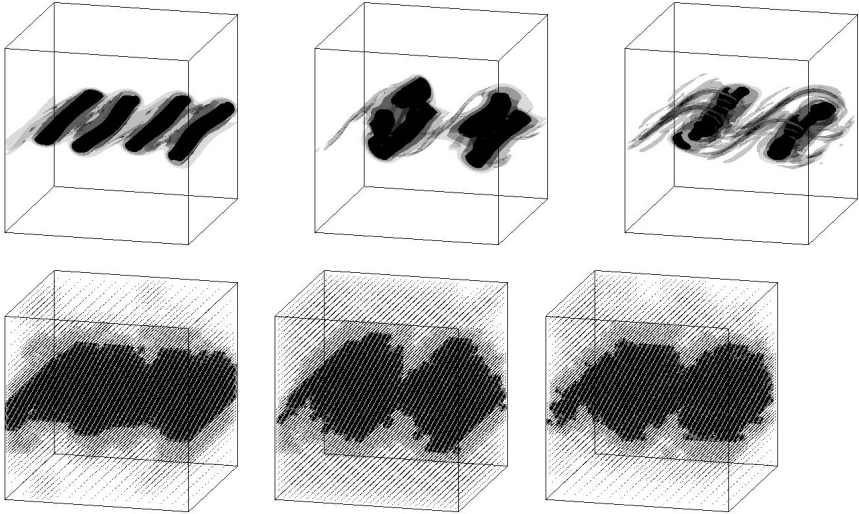
Fig. 4 CVS of a 3D compressible mixing layer, $Ma = 0.3$, $Re = 200$. Top: isosurfaces of vorticity $||\omega|| = 0.6$ (*black*), $||\omega|| = 0.4$ (*dark gray*), and $||\omega|| = 0.2$ (*light gray*) at $t = 18$, (*left*) $t = 37$ (*center*), and $t = 80$ (*right*). Bottom: corresponding adaptive grids

explicit second-order Runge-Kutta scheme. The wavelet basis used for the filtering relies on the cell-average multiresolution analysis developed by Harten [19]. After the filtering, the discarded coefficients are removed from memory, so that both CPU time and memory requirements are significantly reduced in comparison with the DNS computation. The data structure is organized into a graded-tree form to be able to navigate through it. To perform the CVS computations, a three-dimensional adaptive multiresolution algorithm [30], originally developed for reaction-diffusion equations, has been extended to the compressible Navier-Stokes equations. Extensions of the adaptive multiresolution scheme to the compressible Euler equations can be found in [6].

As example, we apply the CVS method here to compute a time-developing three-dimensional turbulent mixing layer in the weakly compressible regime. CVS computations of incompressible turbulent mixing layers have been presented in [32]. In this test-case, both layers have the same initial velocity norm, but opposite directions. An initial three-dimensional sinusoidal perturbation is added to the basic profile. The Reynolds and Mach numbers, based on the initial velocity norm and

half the initial layer thickness, are set to 200 and 0.3, respectively. The results are compared with the one obtained by DNS performed on the regular finest grid with the same numerical scheme. We find that only 17.9 % wavelet coefficients contain around 98.3 % of the energy and 93.4 of the enstrophy. Taking into account all the nodes of the tree data structure, these wavelet coefficients represent 30.2% of the $128^3 = 2097152$ cells that the fine-grid computation requires. Concerning the CPU time, it only represents 29.0% of the one required by the DNS, i.e. CVS is in the present case three times faster than DNS.

These results show that the CVS method yields accurate results in comparison with DNS, while significantly reducing the CPU time and memory requirements. Further work will focus on the CVS of compressible mixing layers with larger values of both Mach and Reynolds numbers, i.e. in a more turbulent and more compressible regime, for which higher compression of memory and CPU time are expected, cf. [31].

4 Adaptive Multiresolution Methods for Evolutionary PDEs

Up to now, different approaches have been investigated to define adaptive space discretizations, some emerge from *ad hoc* criteria, others are based on more elaborated *a posteriori* error estimators using control strategies by solving computational expensive adjoint problems.

In the framework of the current project we focused on multiresolution based schemes (MR) for evolutionary PDEs. The multiresolution data representation is the main idea of the MR method. The decay of the MR coefficients gives information on local regularity of the solution. Therewith the truncation error can be estimated and coarser grids can be used in regions where this error is small and the solution is smooth. An adaptive grid can be introduced by suitable thresholding of the multiresolution representation where only significant coefficients are retained.

Hence a given discretization on a uniform mesh can be accelerated as the number of costly flux evaluations is significantly reduced, while maintaining the accuracy of the discretization. The memory requirement could also be reduced, for example using a dynamic tree data structure.
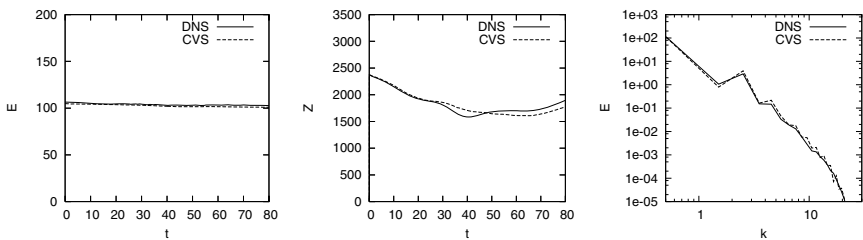

Fig. 5 Comparison between DNS and CVS of a 3D compressible mixing layer, $Ma = 0.3$, $Re = 200$. Left: time evolution of energy. Center: time evolution of enstrophy. Right: energy spectra at $t = 80$
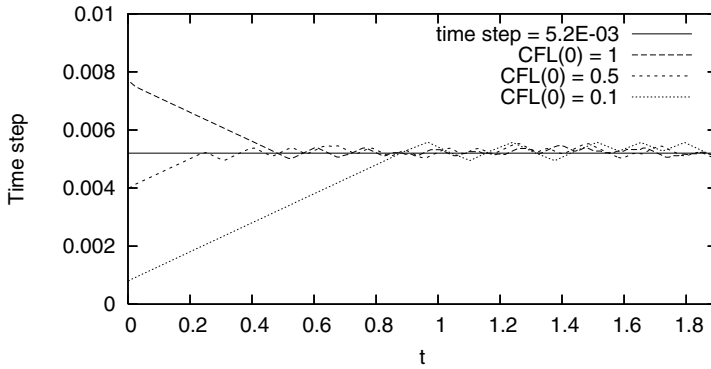
Fig. 6 Evolution of the time step depending on the initial CFL value for the finite volume scheme with global time adaptivity using the RKF 2(3) method for the advection equation. Grid containing 256 points, $\delta_{desired} = 10^{-3}$, $\mathscr{S}_0 = 0.01$
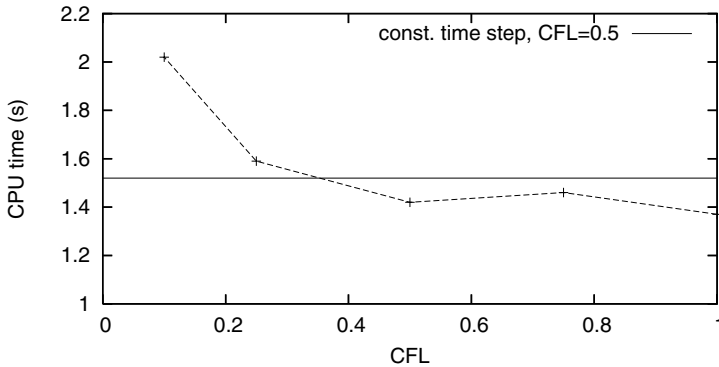

Fig. 7 CPU time vs. initial CFL value for the advection equation. The grid contains 256 points. The parameters are $\delta_{desired} = 10^{-3}$, $\mathscr{S}_{min} = 0.01$, and $\mathscr{S}_0 = 0.10$

A main bottleneck of most of these space–adaptive methods, which typically employ explicit or semi–explicit time discretizations, is that the finest spatial grid size imposes a small time step in order to fulfill the stability criterion of the time scheme. Hence, for extensive grid refinement with a huge number of refinement levels, a very small size of the time step is implied.

The aim in the present project was to develop local scale dependent time stepping for the space adaptive multiresolution scheme introduced in [30]. The idea is to obtain additional speed up of this efficient space adaptive scheme by introducing at large scales larger time steps without violating the stability condition of the explicit time scheme and less flux evaluation due to larger time steps. The originality of our work is to combine, in the framework of the cell-average multiresolution analysis, a local time stepping together with multi-stage Runge-Kutta methods. The
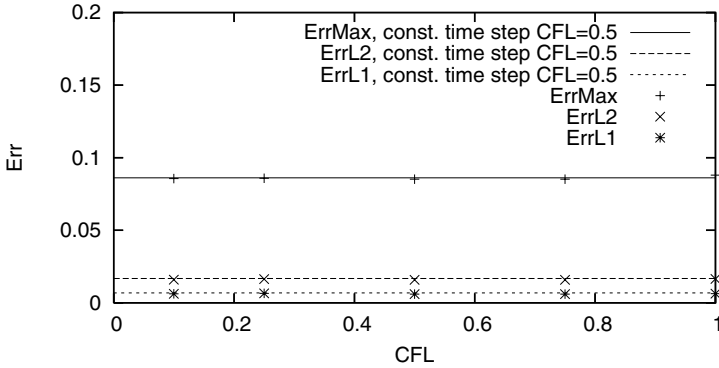
Fig. 8 Errors vs. initial CFL value for the advection equation. The grid contains 256 points. The parameters are $\delta_{desired} = 10^{-3}$, $\mathscr{S}_{min} = 0.01$, and $\mathscr{S}_0 = 0.10$
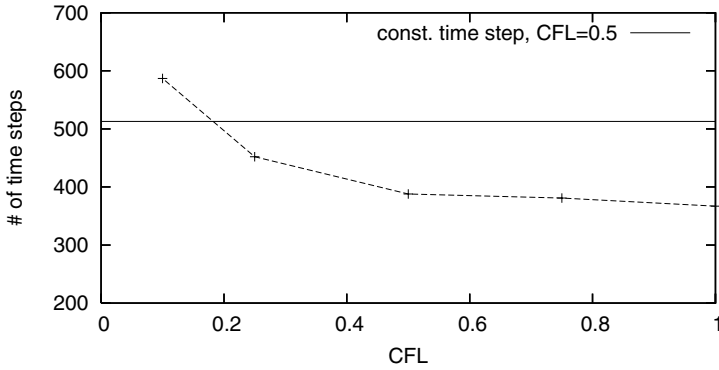

Fig. 9 Number of time steps vs. initial CFL value for the advection equation. The grid contains 256 points. The parameters are $\delta_{desired} = 10^{-3}$, $\mathscr{S}_{min} = 0.01$, and $\mathscr{S}_0 = 0.10$

synchronization we propose differs from the one introduced in [25], where single-stage methods were used.

Starting point of our work is the fully adaptive numerical scheme for evolutionary PDEs in Cartesian geometry which based on a second order finite volume discretization. A multiresolution strategy allows local grid refinement while controlling the approximation error in space. The number of costly flux evaluations is significantly reduced. For details we refer the reader to [30]. For time discretization we use an explicit Runge-Kutta scheme of second order with a scale dependent time step. On the finest scale the size of the time step is imposed by the stability condition of the explicit scheme. On large scales the time step can be increased without severe violation of the stability requirement of the explicit scheme. The implementation uses a dynamic tree data structure which allows memory compression and CPU time reduction. In [6] we present numerical validations for test problems in one space dimension which demonstrate the efficiency and accuracy of the local time stepping

scheme with respect to both the multiresolution scheme with global time stepping and the finite volume scheme on a regular grid. Fully adaptive three-dimensional computations for reaction-diffusion equations illustrated the memory reduction and the CPU speed-up for a flame instability. For details we again refer the interested reader to [6].

In [6, 7] we extended the above scheme and developed an adaptive time stepping scheme with automatic error control. The adaptive time integration method is based on a Runge–Kutta–Fehlberg method, which allows an estimation of the local error in time. An original limiting technique is also proposed to avoid non admissible choices for the time step. The adaptivity in space is done through a multiresolution method, which automatically detects the local regularity of the solution and hence guarantees automatic grid adaption in space. The costly numerical fluxes are evaluated on this locally refined, while ensuring strict conservativity. The implementation uses graded tree data structures which allows an efficient representation of the solution on adaptive grids with reduced memory requirements. Applications are shown for the compressible Euler equations [6].

4.1 Advection Equation in 1D

As example (see [7]) we consider the linear advection equation

$$\frac{\partial u}{\partial t} + c\frac{\partial u}{\partial x} = 0,$$

where $u = u(x,t)$, $t \geq 0$, $(x,y) \in [-\frac{1}{2}, \frac{1}{2}]$, and $c > 0$ is the constant velocity. The boundary conditions are periodic and the initial condition is

$$u(x,0) = \exp\left(-50x^2\right).$$

The elapsed time is set to $t = 1$, so that the final solution is equal to the initial one.

In Figure 6, we show the time evolution of the time step for different initial CFL values, i.e., for different initial time step sizes, using the finite volume scheme on a regular grid with global time adaptivity and the RKF 2(3) method. We observe that the time steps tend to converge in all cases to a time step around 5.2×10^{-3}. To avoid a "bad choice" of the initial CFL values, the code allows a bigger limiter in the beginning time steps. These "bad choices" of initial CFL could however increase the global error, as presented in Table 4. The automatic step size control of the solution reduces the number of time steps and hence the computational cost (cf. Table 4). We can also observe that the final error with respect to the analytical solution is reduced for the time adaptive schemes, compared to the finite volume scheme with fixed time stepping, except for the initial CFL = 1 using the L^∞ norm.

In Figure 8, we compare L^2, L^1, L^∞ norms for the RK 3 method with CFL = 0.5 and the RKF 2(3) method. The results show that the choice of the initial time step does not influence the final error, since all computations yield a similar result. Figure 7 shows the CPU time spent for different choices of the initial CFL. The CPU

Table 4 Initial CFL, number of time steps, CPU time, initial and final time steps, and errors for the advection equation. Mesh containing 256 points, $\delta_0 = 10^{-3}$, $\mathscr{S}_{min} = 0.01$, $\mathscr{S}_0 = 0.10$. The first line corresponds to the constant time step with CFL=0.5

Init. CFL	# steps	% CPU compression	Initial time step	Final time step	L^∞-error	L^2-error	L^1-error
0.50	513	100	3.91e-03	3.91e-03	8.61e-02	1.68e-02	6.84e-03
1.00	367	90	7.64e-03	5.27e-03	8.80e-02	1.65e-02	6.27e-03
0.75	381	96	5.73e-03	5.18e-03	8.52e-02	1.58e-02	5.97e-03
0.50	388	93	3.90e-03	5.15e-03	8.52e-02	1.58e-02	5.97e-03
0.25	452	105	2.00e-03	4.88e-03	8.58e-02	1.64e-02	6.57e-03
0.10	587	133	7.98e-04	4.94e-03	8.56e-02	1.60e-02	6.23e-03

time decreases as the initial CFL increases. This is directly related to the number of time steps needed to compute the solution at $t = 1$, as could be observed in Fig. 9. For this test case, we can thus conclude that RKF 2(3) is more efficient than the conventional RK 3 method with a fixed time step.

5 Wavelet Decomposition for LES - Implementation in the LESOCC2 Code

All simulations of the test cases presented further have been performed with the block-structured finite volume code LESOCC2 [20]. In this code the wavelet decomposition was implemented and used to derive subgrid-scale models for LES. Details are given in [4, 5]. Performing this work in the code LESOCC2 had the advantage of employing an already parallelized code which runs efficiently on a large number of processors with disrtibuted memory access [3].

5.1 Wavelet Subgrid-Scale Modelling

The wavelet decomposition used here is based on Hartens biorthogonal approach [18, 29]. It is applied here to generate a two-level decomposition to obtain the wavelet details . The details from this wavelet decomposition are then used to derive an eddy-viscosity subgrid-scale model in the framework of LES according to the following equation:

$$v_t = C(Vol_p)^{(1/3)} \sqrt{[detail(u)]^2 + [detail(v)]^2 + [detail(w)]^2}. \tag{3}$$

Here, C denotes a model constant which was set equal to 0.02 based on calibration for turbulent channel flow. The quantity Vol_p is the volume of the computational cell on the finer grid, while u, v and w denote the instantaneous values of the velocity components. The above equation was derived based on dimensional reasoning. Alternatively, this model can be obtained in analogy to the structure-function model [23] by substituting the structure functions with the wavelet-details. Further

exploitation of the idea of wavelet decompositions and how they can be used in the framework of LES with mixing of passive scalars is given in [4].

5.2 Numerical Details for the Simulated Cases

The finite-volume code LESOCC2 developed at the University of Karlsruhe for Large Eddy Simulations of incompressible flows uses second-order central schemes for the spatial discretization of all terms. The time-marching is explicit and is based on a second-order Runge-Kutta scheme. The time step is variable computed with a CFL number equal to 0.6. The grid is block-structured, hexahedral, collocated and curvilinear.

Whenever possible a wall-resolving grid was applied for the flow regions close to rigid walls. The Smagorinsky model was used with model constant $C_s = 0.1$ and a van Driest damping function. With the above wavelet model, no wall damping was used. For the cases where the grid near the wall was too coarse to be wall-resolving, the Werner-Wengle wall function was employed for the Smagorinsky model, while for the wavelet-based model the no-slip boundary condition was applied.

6 Complex Flows Simulation: Presentation of Test Case Results

In the framework of the DFG-CNRS cooperation of FOR 507, several test cases were defined to assess LES model development for complex flows. The following cases were computed in the present project and will be discussed below:

- Plane turbulent channel flow with Reynolds numbers $Re_\tau = 180$, 395 and 590;
- Periodic hill flow, $Re = 10\,600$ and $Re = 37\,000$;
- Flow in a model combustor with swirl, $Re = 50\,500$, swirl number $S = 0.6$.

In all subsequent Figures the wavelet model (3) is labeled as "present". Computations with the Smagorinsky model were undertaken with all other parameters unchanged in order to provide sound reference data for the evaluation of the performance of the new model. For the hill flow at the lower Reynolds number, the fine-grid LES solution of Breuer [1] obtained on a grid with $12 Mio$ cells is used as an additional reference data set (REF-MB).

6.1 Plane Channel Flow

The numerical grid consists of about 250,000 control volumes, and is the same for all three Reynolds numbers. As a result, the first node (cell center) in the wall-normal direction is positioned at $y^+ = 1.34$ for $Re_\tau = 180$, at $y^+ = 2.94$ for $Re_\tau = 395$, and at $y^+ = 4.40$ for $Re_\tau = 590$. For the two higher Reynolds numbers, computations with the present model were carried out also with a finer, wall-resolving grid with about 400,000 control volumes. This finer grid resulted in
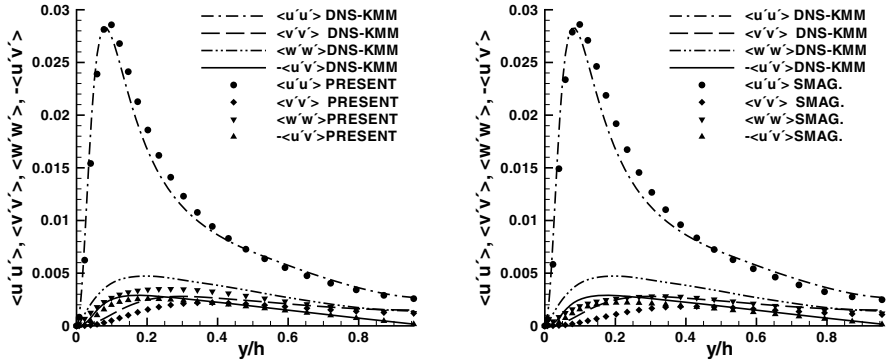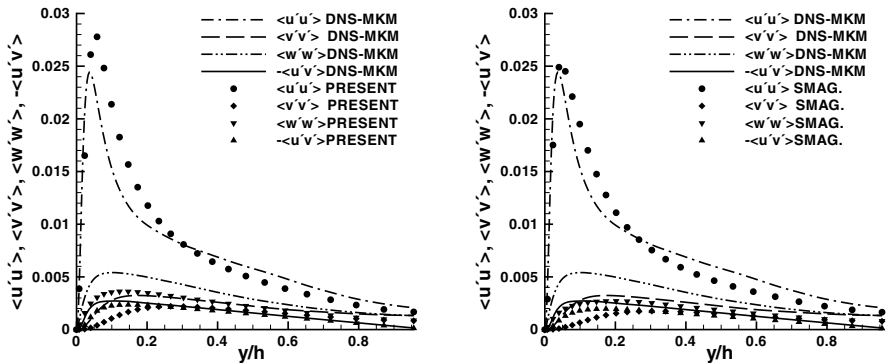
Fig. 10 Resolved turbulent stresses, $Re_\tau = 180$. Left: Present subgrid-scale model compared to the DNS data from [22]. Right: The Smagorinsky model compared to the DNS data from [22]

only very minor improvement so that they are not reproduced here for the sake of brevity.

Results for the resolved Reynolds stresses from the present model and from the Smagorinsky model are compared with DNS data from [22, 24] and presented in Figures 10 to 12. For the lowest Reynolds number the present model is clearly superior to the Smagorinsky model for all turbulence quantities. For $Re_\tau = 395$ and $Re_\tau = 590$ the present model overpredicts the streamwise stresses $\langle u'u' \rangle$, while the Smagorinsky model predicts them with a good accuracy. However, the position of the peak with respect to the y/h coordinate is well predicted by both models. For all other quantities (and especially for the shear stresses $\langle u'v' \rangle$) the present model is superior to the Smagorinsky model.

Fig. 11 Resolved turbulent stresses, $Re_\tau = 395$. Left: Present subgrid-scale model compared to the DNS data from [24]. Right: The Smagorinsky model compared to the DNS data from [24]
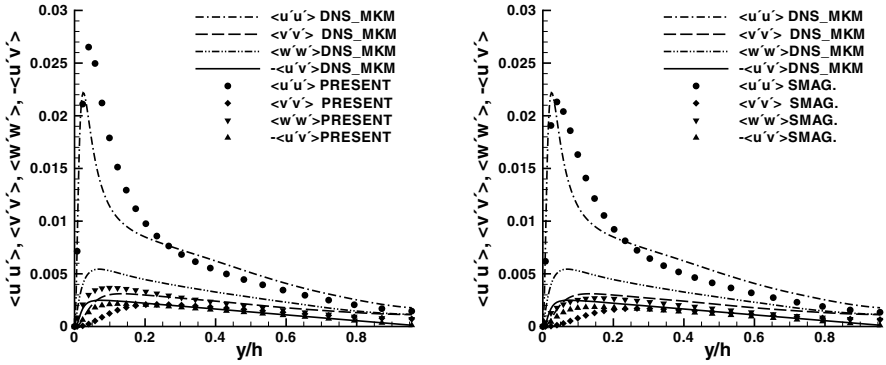
Fig. 12 Resolved turbulent stresses, $Re_\tau = 590$. Left: Present subgrid-scale model compared to the DNS data from [24]. Right: The Smagorinsky model compared to the DNS data from [24]

6.2 Periodic Hill Flow

The periodic hill flow test case was calculated for two different Reynolds numbers. Comparison is performed with data from other groups of the $DFG - CNRS$ collaboration, both numerical [1] and experimental [28]. Fig. 13 shows the geometry and computed streamlines. Configuration and physical issues of this test case are discussed in [16]. In [34], SGS and wall-modelling issues were investigated. The numerical grid employed consists of about $1 Mio$ control volumes. Details are provided in Table 5.

Figure 14 shows the dimensionless streamwise velocity for all models and the experiments at the lower Reynolds number 10595. Compared to the experiments of [28], all numerical simulations overpredict the maximal streamwise velocity by a small amount with the deviation being largest for the present model. In the same Figure data for the resolved turbulent stresses are compared. Here, the new simulations show good agreement with the experimental and numerical reference data. The observed deviations are substantially smaller than those between different SGS models in [34].
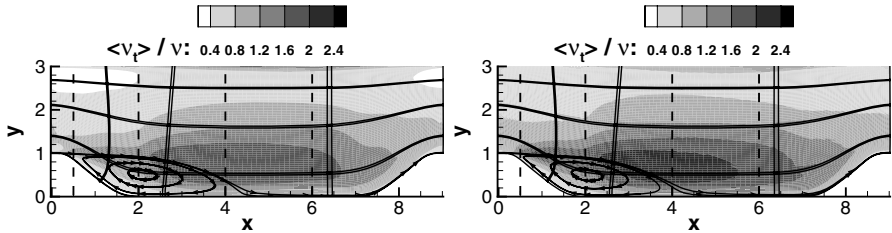

Fig. 13 Streamlines of the averaged flowfield and time-averaged turbulent viscosity, Re=37000. Left: Smagorinsky, Right: Present. Broken vertical lines indicate positions of profiles discussed below. Double lines identify block boundaries of the block-structured grid employed

Table 5 Summary of the numerical simulations of the periodic hill flow. Index "s" - separation point, index "r" - reattachment point, t_a is averaging time and t_x is flow-trough time, LR stands for Re=10595 and HR - for Re=37000

Case	Grid	$\Delta t U_b/h$	t_a/t_x	$(x/h)_s$	$(x/h)_r$
REF-MB (DSM) LR	$281 \times 222 \times 200$	0.0018	141	0.190	4.69
Smagorinsky LR	$160 \times 100 \times 60$	0.0084	72	0.211	4.56
Present LR	$160 \times 100 \times 60$	0.0085	72	0.209	4.86
Smagorinsky HR	$160 \times 100 \times 60$	0.0083	73	0.234	4.62
Present HR	$160 \times 100 \times 60$	0.0079	73	0.294	4.33
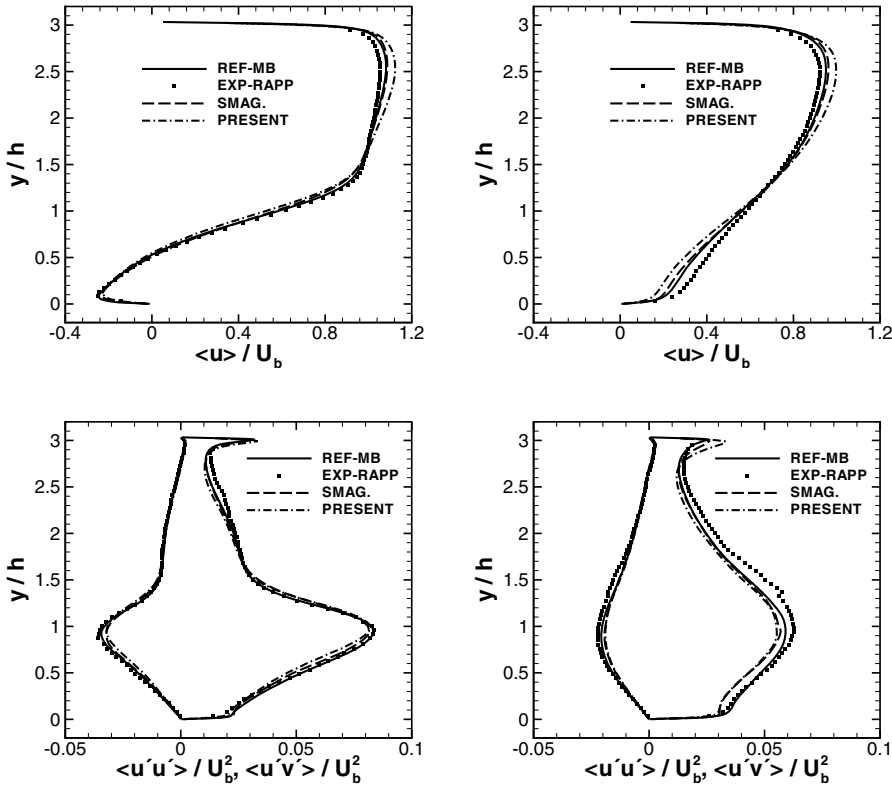
Fig. 14 Comparison of results for $Re = 10595$. $REF - MB$ are reference data on a fine numerical grid from [1]. $EXP - RAPP$ are experimental results from [28]. $SMAG$ are own results with the Smagorinsky model. Left: $x/h = 2$. Right: $x/h = 6$

We now turn to the position $x/h = 0.5$ located at the beginning of the recirculation zone, with corresponding data shown in Fig. 15. As above, the numerical solutions slightly underpredict the mean streamwise velocity in the lower part of the domain ($y/h < 1.8$), while yielding somewhat larger values in the upper part. Concerning
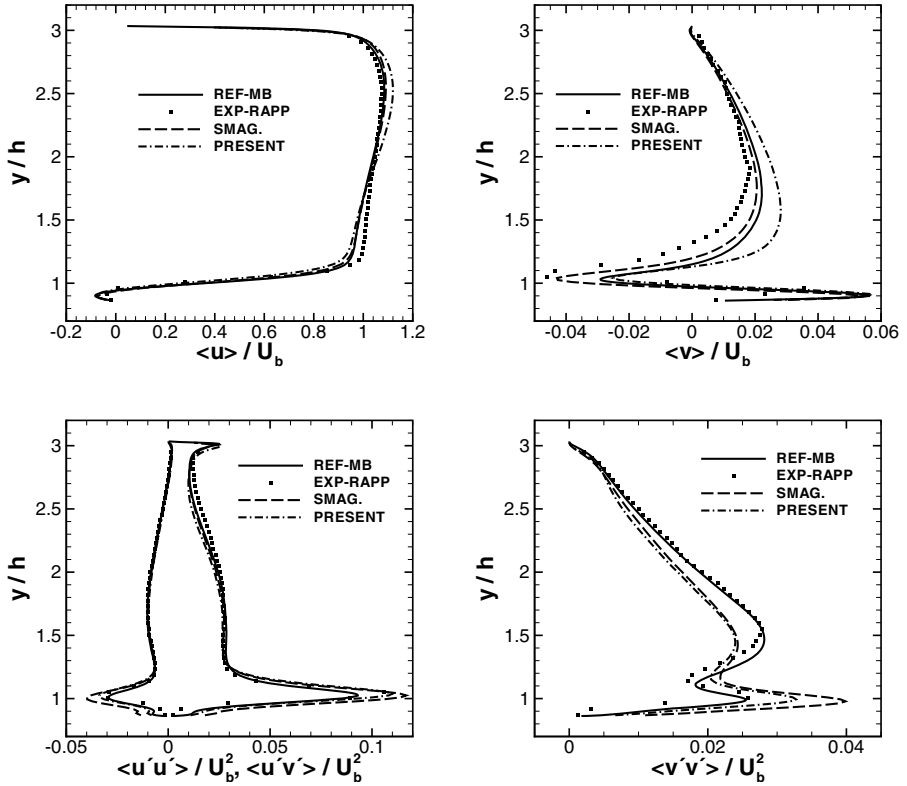
Fig. 15 Comparison of results for $Re = 10595$ at $x/h = 0.5$. For additional explanations see caption of Fig. 14

the vertical velocity component $\langle v \rangle$, it is to be observed that its value is substantially smaller than $\langle u \rangle$, so that differences should not be over-interpreted. Closest to the experiments are the data obtained with the Smagorinsky model, while the present model yields larger values. The resolved Reynolds stresses in the lower pictures of the figure agree very well with the reference data. Here, $\langle v'v' \rangle$ exhibits the largest visual differences, with the present model and the Smagorinsky model being similar in the upper part and the present model better in the lower part. But again absolute value of $\langle v'v' \rangle$ is small.

In the following Fig. 16 we present results for the hill flow with $Re = 37000$. It is the first time that this case is computed since the experimental data have been obtained only recently. Hence, only the experimental data of [28] are available for comparison. Since the Reynolds number is higher than for the previous case it is expected that the contribution of the SGS-modelling is larger. In order to be able to assess this, a solution without a SGS-model was carried out (referenced as *PDNS* with *P* standing for "Pseudo"). For the mean streamwise velocity, this *PDNS* solution yields results which are closer to the experimental data than obtained with the
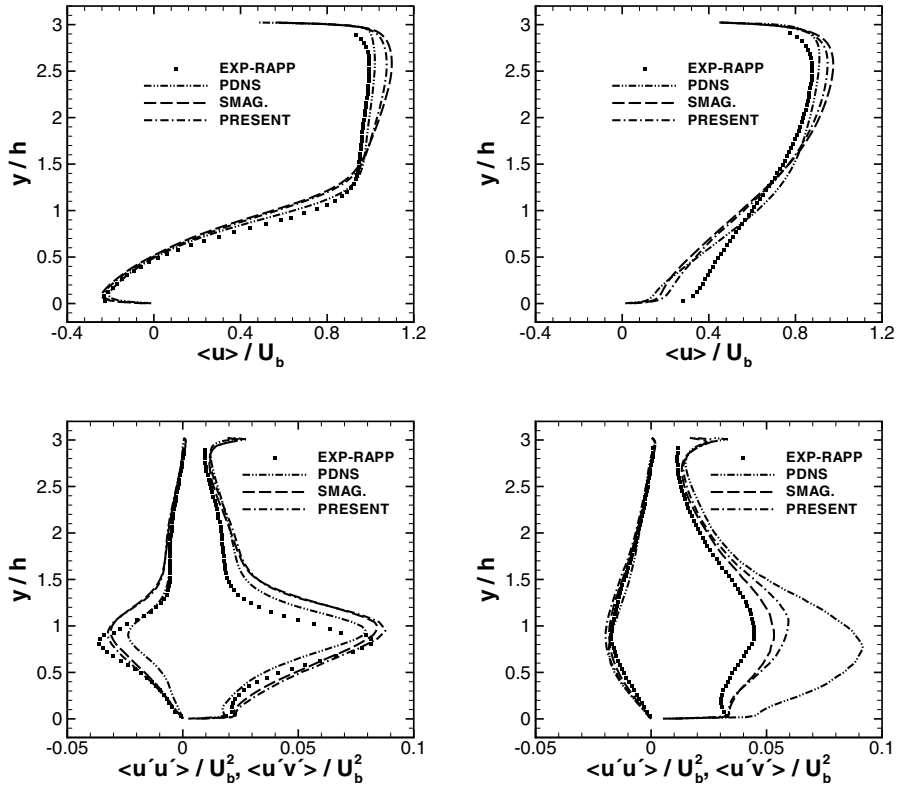
Fig. 16 Comparison of results for $Re = 37000$. Left: $x/h = 2$. Right: $x/h = 6$. For additional explanation see caption of Fig. 14

other simulations. For the resolved Reynolds stresses, however, and in particular for $\langle u'u' \rangle$, the results are worse than those from the other cases. Comparing the results with the new model and the Smagorinsky model shows that the Reynolds stresses are largely the same in both cases. This is even more observed for the mean flow.

The overall analysis carried out so far shows that the agreement between the numerical simulations and the experiments is better for the lower Reynolds number than for the higher one. In order to investigate the effect of the Reynolds number, results for both $Re = 10595$ and $Re = 37000$ are presented in Fig. 17 at $x/h = 4.0$ - a position at which the recirculation zone approximately ends. The mean streamwise velocity $\langle u \rangle$ in the experiment becomes more uniform with increasing Reynolds number. The same trend is observed with the present model, while for the Smagorinsky model the curves are almost identical between the two cases. Concerning the Reynolds stresses it is observed that these, when scaled with U_b^2, decay with increasing Reynolds number in the experiment. The results of the simulations, all obtained on the same grid, are very much alike. Only for $\langle u'u' \rangle$ slight deviations are observed showing a small trend in opposite direction, i.e. increasing scaled fluctuations with
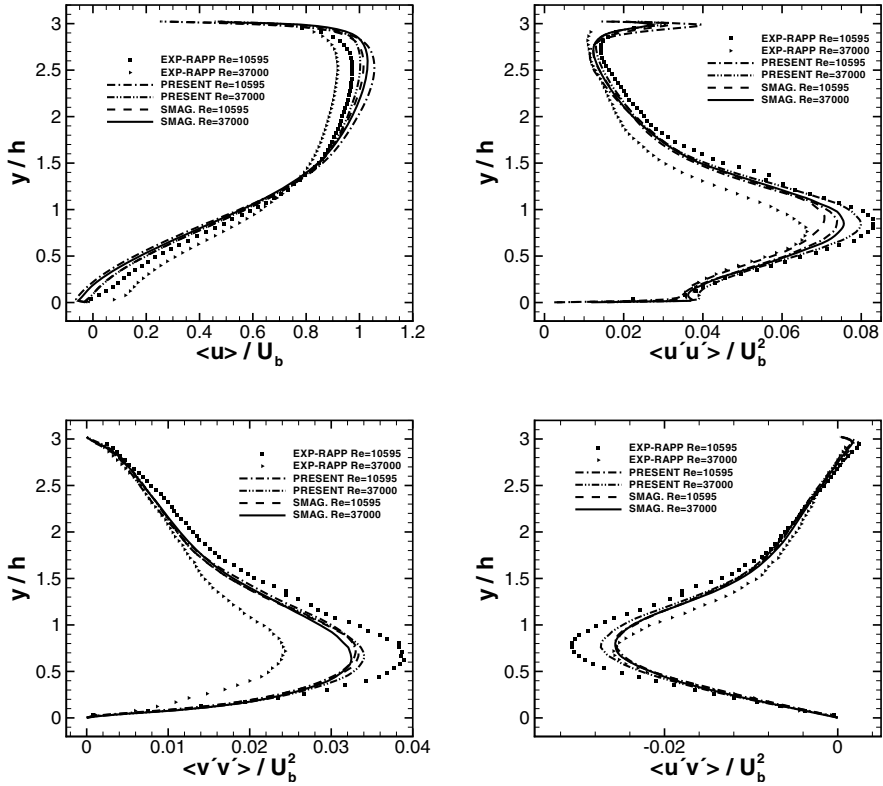
Fig. 17 Comparison of results for the two Reynolds numbers considered, $x/h = 4$. For additional explanations see caption of Fig. 14

Re. In particular, the results of the new model are close to those of the Smagorinsky model. These observations can be related to the mean eddy viscosity displayed in Fig. 13. The change of this quantity with *Re* (not displayed here) is very small. The difference between the two models can be appreciated in that figure for $Re = 37000$ and is about 10-15%.

One time step with the present wavelet model was about 5% faster than the Smagorinsky model with respect to the CPU-time for the cases with Reynolds number 37000. Additional information about the computations performed as well as for the separation and reattachment points is given in Table 5.

6.3 Flow in a Model Combustor with Swirl

The annular swirl combustor experimentally investigated at the Technical University of Darmstadt [27, 33] was another testcase in the DFG-CNRS collaboration. In the following we focus on the burner geometry and compute the flow prior to the outlet into the combustion chamber, as it was done in [27].
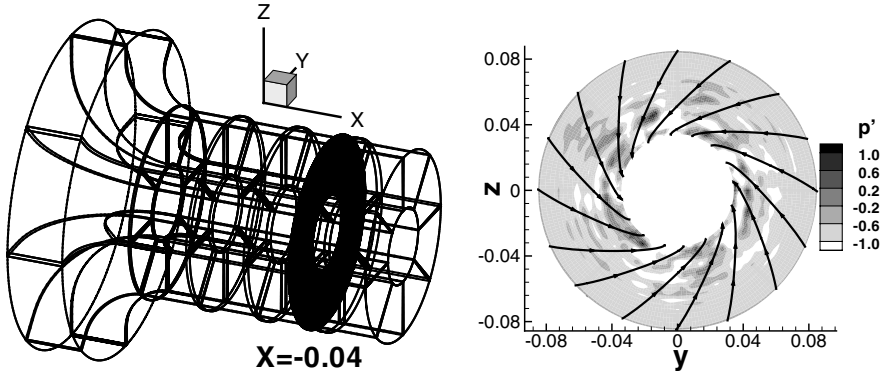
Fig. 18 Numerical blocks with the section $x = -0.04$, where comparison with measurements are presented (left). Inflow section at $x = -0.165$ with the averaged streamlines and instantaneous pressure fluctuation (right)

This annular swirler as depicted in Fig. 18 has an inner wall and an outer wall and no blades. Its dimensions are the following: length $0.180[m]$, radius at the inflow section $0.085[m]$, inner radius of the annulus $r_i = 0.020[m]$ and outer radius $r_o = 0.050[m]$. The Reynolds number based on the hydraulic diameter of the annulus is $Re = 50500$ with a bulk velocity $U_b = 10.94[m/s]$ used as characteristic velocity.

The swirl number in the plane of comparison was to $S = 0.6$ and is visualized by the streamlines of the mean flow in the right graph of Fig. 18. This was achieved with the following values at the inflow boundary of the domain: radial component $4.51[m/s]$ and tangential component $3.01[m/s]$.

The computational grid employed contains 1.9 Mio computational nodes decomposed into 40 blocks as depicted in Fig. 18. The computation was performed over 12.5 flow-through times and averaging was accumulated over 10.5 flow-trough times. Using 20 processors on an HP XC4000 this simulation took approximately 72 hours wall-clock time.

The contour plot in Fig. 18 provides instantaneous data of the pressure fluctuations convey an impression of the structure and the size of turbulent fluctuations at this position.

Figure 19 presents a comparison between numerical and experimental results in the annular swirler, at $x = -0.040[m]$. This section had been selected for measurements in the experiments [27]. From the different simulations carried out in [33], the one with the Dynamic Smagorinsky model and a boundary condition set denoted as "simplified swirler" has been used here for comparison as it corresponds most closely to the present set of boundary conditions and computational domain. In the figures these results are denoted "DSM" and the corresponding experimental data from [33] have been used for comparison, too. The present simulation were undertaken using the Smagorinsky model as well as the new wavelet model.
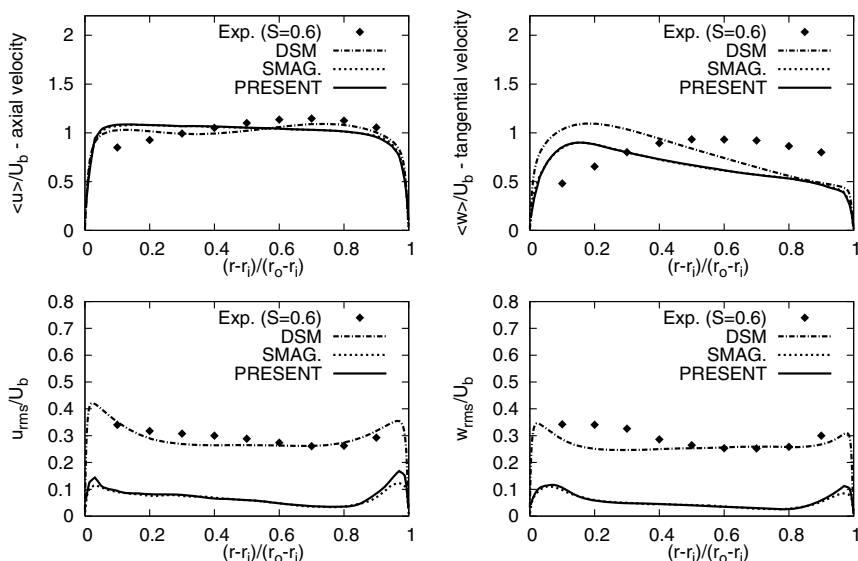
Fig. 19 Comparison of different numerical simulations with experiments at $x = -0.04[m]$. DSM and experimental data courtesy to Šarić and Jakirlić [33]

Figure 19 shows that the DSM simulation of [33] agrees well with the experimental data. The simulations performed in the present paper with the two SGS models considered produced virtually identical data. They yield a mean streamwise velocity profile which is close to the reference data. The deviation for the mean circumferential velocity $\langle w \rangle$ between the present models and the DSM is larger, in particular near the inner wall. The reason for this behavior is the substantially lower level of fluctuations compared to the reference simulation and the experiment. This, in turn, may be due to the use of stationary inflow conditions (in [33] this issue is not discussed). Computations with different boundary conditions and numerical parameters are under way to elucidate this issue.

7 Conclusions

The present paper gives examples of analysis and simulation of complex turbulent flows with a particular emphasis on the utilization of the orthogonal and biorthogonal wavelet decomposition for their study and computation.

Theoretical background and applications of the wavelet based coherent vortex extraction method are presented for homogeneous isotropic turbulence at different Reynolds numbers.

A summary of the developed adaptive multiresolution method for evolutionary PDEs is presented. First fully adaptive computations of 3d mixing layers using Coherent Vortex Simulation are shown. Features like local scale dependent time stepping are also illustrated and examples for one dimensional problems are given.

Computations with the developed wavelet models have been performed on complex geometries and flows with high Reynolds numbers applicable to engineering problems. For this purpose three test cases selected in the present DFG-CNRS cooperation were simulated comprising non-orthogonal grids and swirl. The simulations with the finite-volume code LESOCC2 show that the wavelet-based models are robust and efficient for the purpose of parallel computations, showing a good accuracy when compared to classical subgrid-scale models like the one of Smagorinsky.

References

1. Breuer, M.: New reference data for the Hill Flow Test Case: DFG - CNRS Research Unit 507, A French-German Research Group (2005), http://www.hy.bv.tum.de/DFG-CNRS
2. Daubechies, I.: Ten Lectures on wavelets. In: CBMS-NSF Conferences in Applied Mathematics, vol. 61. SIAM, Philadelphia (1992)
3. Denev, J.A., Fröhlich, J., Bockhorn, H.: Direct Numerical Simulation of a Round Jet into a Crossflow - Analysis and Required Resources. In: Nagel, W.E., Kröner, D., Resch, M. (eds.) Transactions of the High Performance Computing Center, Stuttgart (HLRS), pp. 339–350. Springer, Heidelberg (2007)
4. Denev, J.A., Fröhlich, J., Falconi, C., Bockhorn, H.: Direct Numerical Simulation and Large Eddy Simulation of transport processes in a jet in crossflow. In: Mewes, D., et al. (eds.) Springer series on Heat and Mass Transfer (to appear, 2008)
5. Denev, J.A., Falconi, C., Fröhlich, J., Bockhorn, H.: Wavelet-adapted sub-grid scale models for LES. In: Second International Conference on Turbulence and Interaction, Sainte-Luce, Martinique, 31 May - 5 June (to appear, 2009) (submitted)
6. Domingues, M., Gomes, S., Roussel, O., Schneider, K.: Space-Time adaptive multiresolution methods for hyperbolic conservation laws: Applications to compressible Euler equations. Appl. Num. Math. (April 2008) (accepted)
7. Domingues, M., Roussel, O., Schneider, K.: An adaptive multiresolution method for parabolic PDEs with time-step control. Int. J. Num. Meth. Eng. (October 2008) (accepted)
8. Domingues, M., Gomes, S., Roussel, O., Schneider, K.: An adaptive multiresolution scheme with local timestepping for evolutionary PDEs. J. Comput. Phys. 227, 3758–3780 (2008)
9. Donoho, D.: Unconditional bases are optimal bases for data compression and statistical estimation. Appl. Comput. Harmon. Anal. 1, 100–115 (1993)
10. Donoho, D., Johnstone, I.: Ideal spatial adaption via wavelet shrinkage. Biometrica 81, 425–455 (1994)
11. Farge, M.: Wavelet transforms and their applications to turbulence. Ann. Rev. of Fluid Mech. 24, 395–457 (1992)
12. Farge, M., Schneider, K., Kevlahan, N.: Non-gaussianity and coherent vortex simulation for two-dimensional turbulence using an adaptive orthonormal wavelet basis. Phys. Fluids 11(8), 2187–2201 (1999)
13. Farge, M., Pellegrino, G., Schneider, K.: Coherent vortex extraction in 3D turbulent flows using orthogonal wavelets. Phys. Rev. Lett. 87(5), 054501 (2001)

14. Farge, M., Schneider, K.: Coherent vortex simulation (CVS), a semi-deterministic turbulence model using wavelets. Flow, Turbulence and Combustion 66(4), 393–426 (2001)
15. Farge, M., Schneider, K., Pellegrino, G., Wray, A.A., Rogallo, R.S.: Coherent vortex extraction in three-dimensional homogeneous turbulence: comparision between CVS-wavelet and POD-Fourier decompositions. Phys. Fluids 15(10), 2886–2896 (2003)
16. Fröhlich, J., Mellen, C.P., Rodi, W., Temmerman, L., Leschziner, M.A.: Highly resolved large-eddy simulation of separated flow in a channel with streamwise periodic constrictions. J. Fluid Mech. 526, 19–66 (2005)
17. Gottlieb, D., Turkel, E.: Dissipative two-four methods for time-dependent problems. J. Comput. Phys. 30, 703–723 (1976)
18. Harten, A.: Discrete multi-resolution analysis and generalized wavelets. J. Appl. Num. Math. 12, 153–193 (1993)
19. Harten, A.: Multiresolution algorithms for the numerical solution of hyperbolic conservation laws. Comm. Pure Appl. Math. 48, 1305–1342 (1995)
20. Hinterberger, C.: Three-dimensional and depth-averaged Large-Eddy-Simulation of flat water flows. PhD thesis, Inst. Hydromechanics, Univ. of Karlsruhe, 296 p. (2004)
21. Jeong, J., Hussain, F.: On the identification of a vortex. J. Fluid Mech. 285, 69–94 (1995)
22. Kim, J., Moin, P., Moser, R.: Turbulence statistics in fully developed channel flow at low Reynolds number. J. Fluid Mech. 177, 133–166 (1987)
23. Métais, O., Lesieur, M.: Spectral large-eddy simulations of isotropic and stably-stratified turbulence. J. Fluid Mech. 239, 157–194 (1992)
24. Moser, R., Kim, J., Mansour, N.: Direct numerical simulation of turbulent channel flow up to Re_{tau} = 590. Phys. Fluids 11, 943–945 (1999)
25. Müller, S., Stiriba, Y.: Fully adaptive multiscale schemes for conservation laws employing locally varying time stepping. J. Sci. Comput. 30(3), 493–531 (2007)
26. Okamoto, N., Yoshimatsu, K., Schneider, K., Farge, M., Kaneda, Y.: Coherent vortices in high resolution direct numerical simulation of homogeneous isotropic turbulence: A wavelet viewpoint. Phys. of Fluids 19, 115109 (2007)
27. Palm, R., Grundmann, S., Weismüller, M., Šarić, S., Jakirlić, S., Tropea, C.: Experimental characterisation and modelling of inflow conditions for a gas turbine swirl combustor. Int. J. Heat Fluid Flow 27, 924–936 (2006)
28. Rapp, C.: Experimentelle Studie der turbulenten Strömung über periodische Hügel', Dissertation, Technische Universität München (2008)
29. Roussel, O.: Development of an multiresolution adaptive three-dimensional algorithm for the solution of parabolic partial differential equations. Application to thermo-diffusive flame instabilities. Ph.D. Thesis, University of Aix-Marseille II, 147 p. (2003)
30. Roussel, O., Schneider, K., Tsigulin, A., Bockhorn, H.: A conservative fully adaptive multiresolution algorithm for parabolic PDEs. J. Comput. Phys. 188(2), 493–523 (2003)
31. Roussel, O., Schneider, K.: Coherent Vortex Simulation of compressible turbulent mixing layers using adaptive multiresolution methods. J. Comput. Phys. (submitted, 2008)
32. Schneider, K., Farge, M., Pellegrino, G., Rogers, M.: Coherent vortex simulation of three–dimensional turbulent mixing layers using orthogonal wavelets. J. Fluid Mech. 534, 39–66 (2005)
33. Šarić, S., Jakirlić, S., Čavar, D., Kniesner, B., Altenhöfer, P., Tropea, C.: Computational study of mean flow and turbulence strucutre in inflow system of a swirl combustor. In: Friedrich, R., et al. (eds.) Procs. of 5th Int. Symp. on Turbulence and Shear Flow Phenomena, TU-Munich, Garching, Germany, August 27-29, vol. 2, pp. 911–918 (2007)
34. Temmerman, L., Leschziner, M.A., Mellen, C.P., Fröhlich, J.: Investigation of wall-function approximations and subgrid-scale models in LES of separated flow in a channel with streamwise periodic constrictions. Int. J. Heat Fluid Flow 24, 157–180 (2005)
35. Yeung, P.K., Donzis, D.A., Sreenivasan, K.R.: High-Reynolds-number simulation of turbulent mixing. Phys. of Fluids 17, 081703 (2005)